



JGR Solid Earth

RESEARCH ARTICLE

10.1029/2023JB027224

Key Points:

- Deep crystallization depths
 (~32 ± 7.8 km) and a deep
 axial magma chamber (AMC)
 (~13 ± 7.8 km) may exist under the
 ultraslow-spreading Southwest Indian
 Ridge (SWIR)
- The ascent rate from the AMC to seafloor of the SWIR is ~0.002-0.01 m/s, which is the slowest in global mid-ocean ridge systems
- Magma ascent rates correlate positively with the spreading rates in the global mid-ocean ridge systems

Supporting Information:

Supporting Information may be found in the online version of this article.

Correspondence to:

P.-P. Liu and Q. Chen, ppliu@pku.edu.cn; qiongchen@tongji.edu.cn

Citation

Ma, B., Liu, P.-P., Dick, H. J. B., Zhou, M.-F., Chen, Q., & Liu, C.-Z. (2024). Trans-lithospheric ascent processes of the deep-rooted magma plumbing system underneath the ultraslow-spreading SW Indian Ridge. *Journal of Geophysical Research: Solid Earth*, 129, e2023JB027224. https://doi. org/10.1029/2023JB027224

Received 5 JUN 2023 Accepted 5 JAN 2024 Corrected 1 JUL 2024

This article was corrected on 1 JUL 2024. See the end of the full text for details.

Author Contributions:

Conceptualization: Ben Ma, Ping-Ping Liu

Data curation: Ben Ma Formal analysis: Ben Ma Funding acquisition: Ping-Ping Liu Investigation: Ben Ma, Ping-Ping Liu Methodology: Ben Ma

Project Administration: Ping-Ping Liu Resources: Henry J. B. Dick

Software: Ben Ma **Supervision:** Ping-Ping Liu, Henry J. B.

Dick, Mei-Fu Zhou

© 2024. American Geophysical Union. All Rights Reserved.

Trans-Lithospheric Ascent Processes of the Deep-Rooted Magma Plumbing System Underneath the Ultraslow-Spreading SW Indian Ridge

Ben Ma¹, Ping-Ping Liu¹, Henry J. B. Dick^{2,3}, Mei-Fu Zhou⁴, Qiong Chen⁵, and Chuan-Zhou Liu⁶

¹Key Laboratory of Orogenic Belts and Crustal Evolution, School of Earth and Space Sciences, Peking University, Beijing, China, ²Department of Geology and Geophysics, Woods Hole Oceanographic Institution, Woods Hole, MA, USA, ³Now an Independent Researcher, ⁴State Key Laboratory of Ore Deposit Geochemistry, Institute of Geochemistry, Chinese Academy of Sciences, Guiyang, China, ⁵School of Ocean and Earth Science, Tongji University, Shanghai, China, ⁶State Key Laboratory of Lithospheric Evolution, Institute of Geology and Geophysics, Chinese Academy of Sciences, Beijing, China

Abstract Processes of magma generation and transportation in global mid-ocean ridges are key to understanding lithospheric architecture at divergent plate boundaries. These magma dynamics are dependent on spreading rate and melt flux, where the SW Indian Ridge represents an end-member. The vertical extent of ridge magmatic systems and the depth of axial magma chambers (AMCs) are greatly debated, in particular at ultraslow-spreading ridges. Here we present detailed mineralogical studies of high-Mg and low-Mg basalts from a single dredge on Southwest Indian Ridge (SWIR) at 45°E. High-Mg basalts (MgO = \sim 7.1 wt.%) contain high Mg# olivine (Ol, Fo = 85-89) and high-An plagioclase (Pl, An = 66-83) as phenocrysts, whereas low-Mg basalts contain low-Mg# Ol and low-An Pl (Fo = 75-78, An = 50-62) as phenocrysts or glomerocrysts. One low-Mg basalt also contains normally zoned Ol and Pl, the core and rim of which are compositionally similar to those in high-Mg and low-Mg basalts, respectively. Mineral barometers and MELTS simulation indicate that the high-Mg melts started to crystallize at \sim 32 ± 7.8 km, close to the base of the lithosphere. The low-Mg melts may have evolved from the high-Mg melts in an AMC at a depth of $\sim 13 \pm 7.8$ km. Such great depths of magma crystallization and the AMC are likely the result of enhanced conductive cooling at ultraslow-spreading ridges. Combined with diffusion chronometers, the basaltic melts could have ascended from the AMC to seafloor within 2 weeks to 3 months at average rates of ~0.002–0.01 m/s, which are the slowest reported to date among global ridge systems and may characterize mantle melt transport at the slow end of the ridge spreading spectrum.

Plain Language Summary Mid-ocean ridges are divergent plate boundaries where asthenospheric mantle undergoes decompressional melting to form basaltic melts and lithospheric mantle. The southwest Indian ridge (SWIR) represents the slowest spreading class of ocean ridges. It is characterized by intermittent volcanism resulting in thin or missing oceanic crust. To better understand the magma dynamics of such specific ridges and their correlation with the spreading rates, we calculated the depth of mineral crystallization in high-Mg and low-Mg basalts collected together and constrained the residence time of individual crystals in the melt through Fe-Mg diffusion profiles. We show that the high-Mg melts started crystallization close to the base of the tectonic plate, and likely partially crystallized in a deep magma chamber in the mantle to form low-Mg magmas prior to eruption to the seafloor. This study determined that the rate at which the melts flowed up through the mantle to the crust was the slowest yet found for any ocean ridges. The mineral dynamics of the ultraslow-spreading SWIR therefore illustrate the critical role of the velocity at which the tectonic plates separate on the formation of magmas at mid-ocean ridges.

1. Introduction

Mid-ocean ridges (MORs) are the most important divergent plate boundaries on Earth with variable volcanic activities leading to growth of young oceanic crust. Mid-ocean ridges were long divided into fast-(>80 mm/yr), intermediate-(55–80 mm/yr), slow-(20–55 mm/yr) (Macdonald et al., 1991), and ultraslow-spreading (<20 mm/yr) (Dick et al., 2003) ones according to the full spreading rates. In general, a roughly positive correlation exists between the spreading rate and the oceanic crustal thickness only for the slowest end of the spreading spectrum (Bown & White, 1994; Reid & Jackson, 1981), where ultraslow-spreading ridges are characterized by thin and



Journal of Geophysical Research: Solid Earth

10.1029/2023JB027224

Validation: Ping-Ping Liu
Visualization: Ben Ma
Writing – original draft: Ben Ma
Writing – review & editing: Ping-Ping
Liu, Henry J. B. Dick, Mei-Fu Zhou,
Qiong Chen, Chuan-Zhou Liu

discontinuous oceanic crust (Cochran et al., 2003; Dick et al., 2003; Michael et al., 2003). The depth of crystallization beneath ultraslow-spreading ridges and the distribution of axial magma chamber(s) (AMCs) compared to faster spreading ridges could be shallower due to the thin crust, or deeper due to thicker lithosphere. Crystallization depths calculated from volatile contents of melt inclusions in olivine phenocrysts are usually less than 6 km, and seldomly reach 10 km (e.g., Colman et al., 2015; Shaw et al., 2010; Wanless & Shaw, 2012; Wanless et al., 2015). So far, the deepest crystallization depth of MOR basaltic melts calculated by volatile contents of plagioclase-hosted melt inclusions from the ultraslow-spreading Gakkel ridge records pressures equal to a depth of ~ 16.4 km (Bennett et al., 2019), similar to the lithospheric thickness in that area (up to ~ 17 km derived from seismicity data; Grevemeyer et al., 2019). Studies using different methods of major element barometer have shown that crystallization can occur at mantle depths (≤600 MPa or ~20 km, Wanless & Behn, 2017; up to 1 GPa, Herzberg, 2004; Michael & Cornell, 1998). These pressures from major element barometers are essentially the integration of polybaric crystallization pathways of different minerals (olivine-plagioclase-augite) and are calculated based on the hypothesis of no crystal-melt reactions, which is not true (e.g., Bennett et al., 2019; Lissenberg & MacLeod, 2016). In particular, the average crystallization depths of MOR magmatic systems calculated from major element barometers seem to increase with decreasing spreading rates (e.g., Grove et al., 1992; Herzberg, 2004; Wanless & Behn, 2017).

AMCs are frequently detected seismically at fast- and intermediate-spreading ridges (Canales et al., 2006; Carbotte et al., 2013; Detrick et al., 1987; Singh et al., 1998), but seldomly at slow- and ultraslow-spreading ridges (Jian et al., 2017; Singh et al., 2006; Sinha et al., 1998). Globally, a roughly negative correlation has been observed between the spreading rates and the depths of the AMCs, primarily at <4 km within the oceanic crust (Chen, 2004; Rubin & Sinton, 2007). The deepest AMC reported so far was observed by seismic waves in the lower crust (~4–9 km) at the Southwest Indian Ridge (SWIR) 50°28'E segment (Jian et al., 2017). Geochemical and mineral-ogical evidence for the existence and depth of AMCs at ultraslow-spreading ridges have seldomly been reported.

This study reports compositionally zoned olivine and plagioclase of mid-ocean ridge basalts (MORBs) dredged by RV Thompson Cruise TN365 on the SWIR (45°E). We establish equilibrium olivine-plagioclase-liquid pairs using Fe-Mg partitioning between olivine and liquids, and An-Ab exchange between plagioclase and liquids. Then we use plagioclase-liquid thermobarometers and Rhyolite-MELTS to constrain the depths of magma crystallization and the AMC. Major element barometers are used as references for crystallization depth. Combined with multi-element (Fe-Mg, Mn, Ni) diffusion chronometers, the residence time of olivine phenocrysts is obtained and the minimum magma ascent rate from AMC to seafloor is calculated.

2. Geological Settings and Samples

The SWIR is a highly oblique ultraslow-spreading ridge lying between southern Africa and Antarctica with a full spreading rate of \sim 14 mm/year and a total length of \sim 7,700 km (Figure 1; Dick et al., 2003; Patriat & Segoufin, 1988). Orthogonal- and oblique- spreading (magmatic and amagmatic) modes alternate along the SWIR (e.g., Cannat, Sauter, Mendel, & Escartín, 2006; Cannat, Sauter, Mendel, Ruellan, et al., 2006; Cannat et al., 2008; Dick et al., 2003; Sauter et al., 2013). In amagmatic segments, the mantle lithosphere is characterized by tectonic extension with almost no magmatic activity, leading to thin or even missing oceanic crust (Cochran et al., 2003; Dick et al., 2003; Michael et al., 2003). In other areas, such as the Dragon Flag Supersegment, the thickness of the crust can reach up to 10 km (Jian et al., 2017; Yu & Dick, 2020).

The Marion Rise, corresponding to the southern oceans geoid high, is the most prominent geomorphological feature of the SWIR, extending ~3,400 km from the Andrew Bain Fracture Zone (FZ) to Melville FZ (Figure 1), the highest point of which is ~858 m below sea level (Zhou & Dick, 2013). Two types of ocean rises, that is, axial rise and rifted rise are identified in that area. Rifted rises are characteristic of the area, though locally axial rises do occur. Axial rises are reflected by high melt flux whereas rifted rises are characterized by low melt flux (Ito & Behn, 2008) with deep rift valleys and abundant uplifted peridotites (Dick & Zhou, 2015; Ito & Behn, 2008; Zhou & Dick, 2013). The Marion hotspot (36°E), located ~256 km south of the SWIR, forms a 1.5-km-high and 70-km-long axial volcano, which has the most voluminous volcanic activity on the rifted rise (Zhou & Dick, 2013). Gravity data indicate that the impact of the Marion hotspot is constrained to the west of the Discovery II FZ (Georgen et al., 1998, 2001).

Mapping and sampling show that almost 50% of the 26,000 km² seafloor surveyed between the Discovery II and Indomed FZs consists of uplifted mantle peridotites (Tivey et al., 2019). The seafloor morphology and magnetic and gravity responses of the ridge segments between the Discovery II and Indomed FZs vary significantly from

MA ET AL. 2 of 17

com/doi/10.1029/2023JB027224 by University Of Alaska Fairbanks,

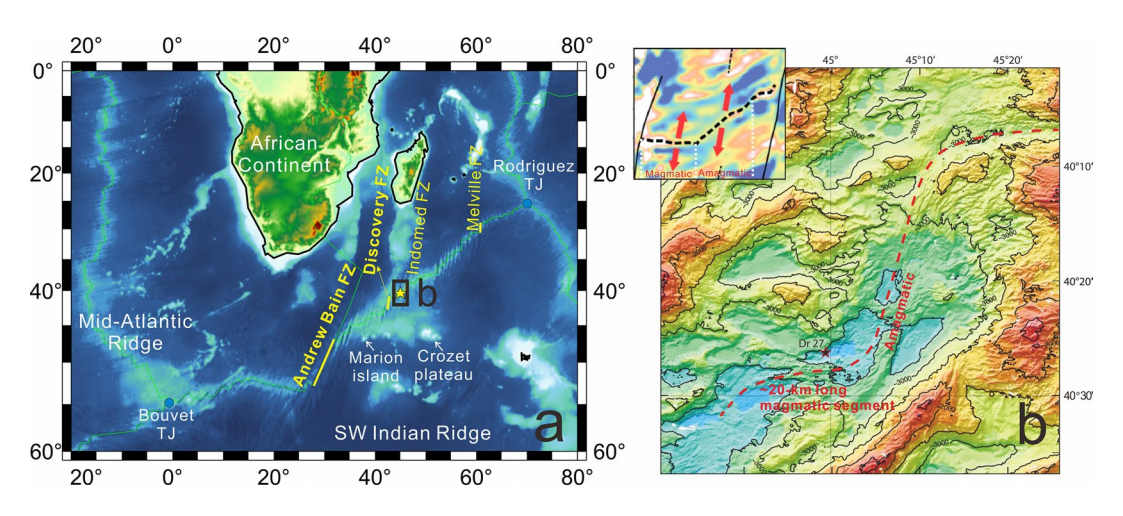


Figure 1. Southwest Indian Ridge (SWIR) bathymetry and dredge location. (a) Bathymetry map of SWIR drawn by The Generic Mapping Tools (Wessel et al., 2019). (b) Location map for Dredge 27 with 500-m contour interval. Oblique highs and lows indicate amagmatic spreading. Illustrations show EMAG2 magnetic anomaly asymmetries. FZ, fracture zone; TJ, triple junction.

west to east (Tivey et al., 2019). The western ridge segment adjacent to the Discovery II FZ and the eastern ridge segment adjacent to the Indomed FZ are magmatic and sandwich an \sim 100-km long oblique amagmatic segment. The basalts in this study were dredged from the north wall of the 20-km long short-lived (\sim 1.4 Ma) magmatic segment at 45°E, 40.5°S centered in the large amagmatic segment (Figure 1b; Zhou et al., 2022).

3. Petrography

The Dredge (Dr.) 27 basalts have porphyritic texture with olivine and plagioclase as the main phenocrysts. Most olivine and plagioclase grains are subhedral and make up ~ 1 and ~ 4 vol.% of the rock, respectively. Most olivine has relatively homogenous composition, whereas plagioclase commonly shows patchy or oscillatory zonation (Figure 2a). In some samples, olivine and plagioclase also form glomerocrysts. One basalt sample, however, contains several normally zoned olivine and plagioclase grains that display resorption textures in their cores (Figures 2e and 2f). The cores of the zoned olivine grains are mostly elliptical and ~ 600 µm in diameter, whereas the rims are dendritic and up to 150 µm wide. The zoned plagioclase grains are irregular in shape with large cores ($\sim 500-2,000$ µm in width) and narrow rims ($\sim 100-500$ µm in width). Anhedral olivine, clinopyroxene, and plagioclase crystallites comprise the matrix (Figure S1 in Supporting Information S1).

4. Methods

4.1. Whole-Rock Major and Trace Element Analyses

Whole-rock major element compositions were determined by X-ray fluorescence spectrometer (XRF) at the School of Earth and Space Sciences, Peking University. The analytical uncertainties are better than 5% for all major elements. Loss-on-ignition (LOI) was determined by heating samples at 950°C for 60 min and recording the percentage of weight loss. Trace elements were measured by inductively coupled plasma-mass spectrometry in the same laboratory. Samples were digested using super-pure HF and HNO₃ (1:1) mixture following the procedures described in Lin et al. (2012). An internal standard solution of 10 ppb Rh was added to monitor signal drift during ion counting. The standards AGV-2, BHVO-2, W-2, and GSP-2 were analyzed together as reference materials. Analytical precisions for most trace elements were better than 3%.

4.2. Electron Microprobe Analyses

Major element contents of the minerals were measured using a JEOL JXA-8100 at the Institute of Geology and Geophysics, Chinese Academy of Sciences (IGGCAS). The analytical conditions were set at an accelerating voltage of 15 kV and a beam current of 20 nA with a spot size of 2 μ m. Peak counting time was 10–30 s. Natural and synthetic oxides were used as standards. The precisions of the major and trace element analyses were better than 2% and 5%, respectively. Matrix corrections were performed by the ZAF procedures.

MA ET AL. 3 of 17

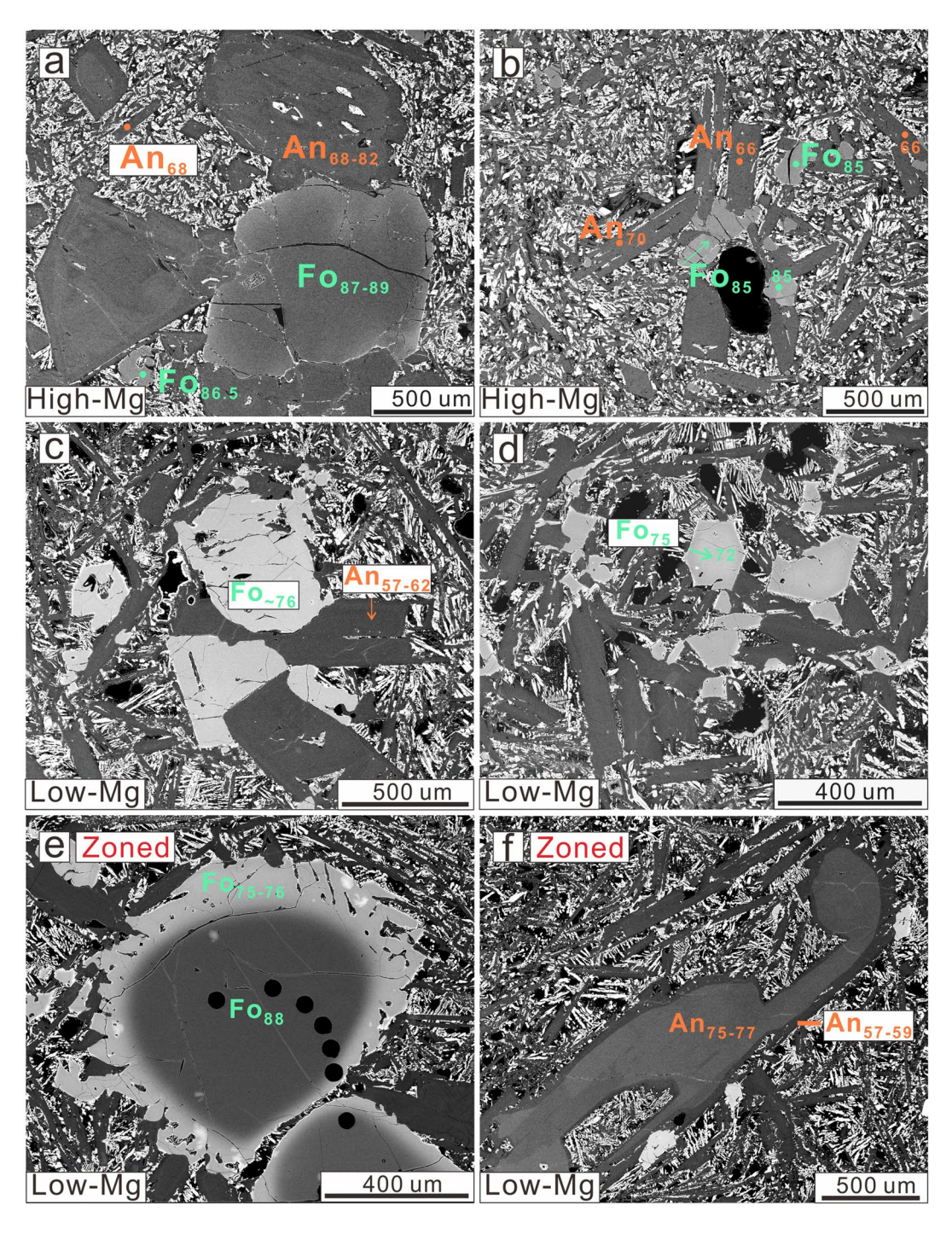


Figure 2. Microphotographs of the 45° E Southwest Indian Ridge basalts. (a) and (b) Plagioclase and olivine phenocrysts in high-Mg basalts. (c) Plagioclase and olivine glomerocrysts in low-Mg basalts. (d) Olivine and plagioclase phenocrysts in low-Mg basalts. (e) Normally zoned olivine grains in low-Mg basalts. (f) Normally zoned plagioclase grains with resorption textures in low-Mg basalts. Fo represents ratios of Mg/(Mg + Fe) \times 100 in olivine and An represents ratios of Ca/ (Ca + Na) \times 100 in plagioclase.

4.3. Electron Backscattered Diffraction (EBSD) Analyses

Electron backscattered diffraction was adopted to measure the crystallographic axis orientation of olivine at the Key Laboratory of Deep-Earth Dynamics of Ministry of Natural Resources, Institute of Geology, Chinese Academy of Geological Sciences. The electron backscatter diffraction patterns were processed using the Stereo32

MA ET AL. 4 of 17

ded from https://agupubs.onlinelibrary.wiley.com/doi/10.1029/2023JB027224 by University Of Alaska Fairbanks, Wiley Online Library on [30/12/2024]. See the Terms and Conditions

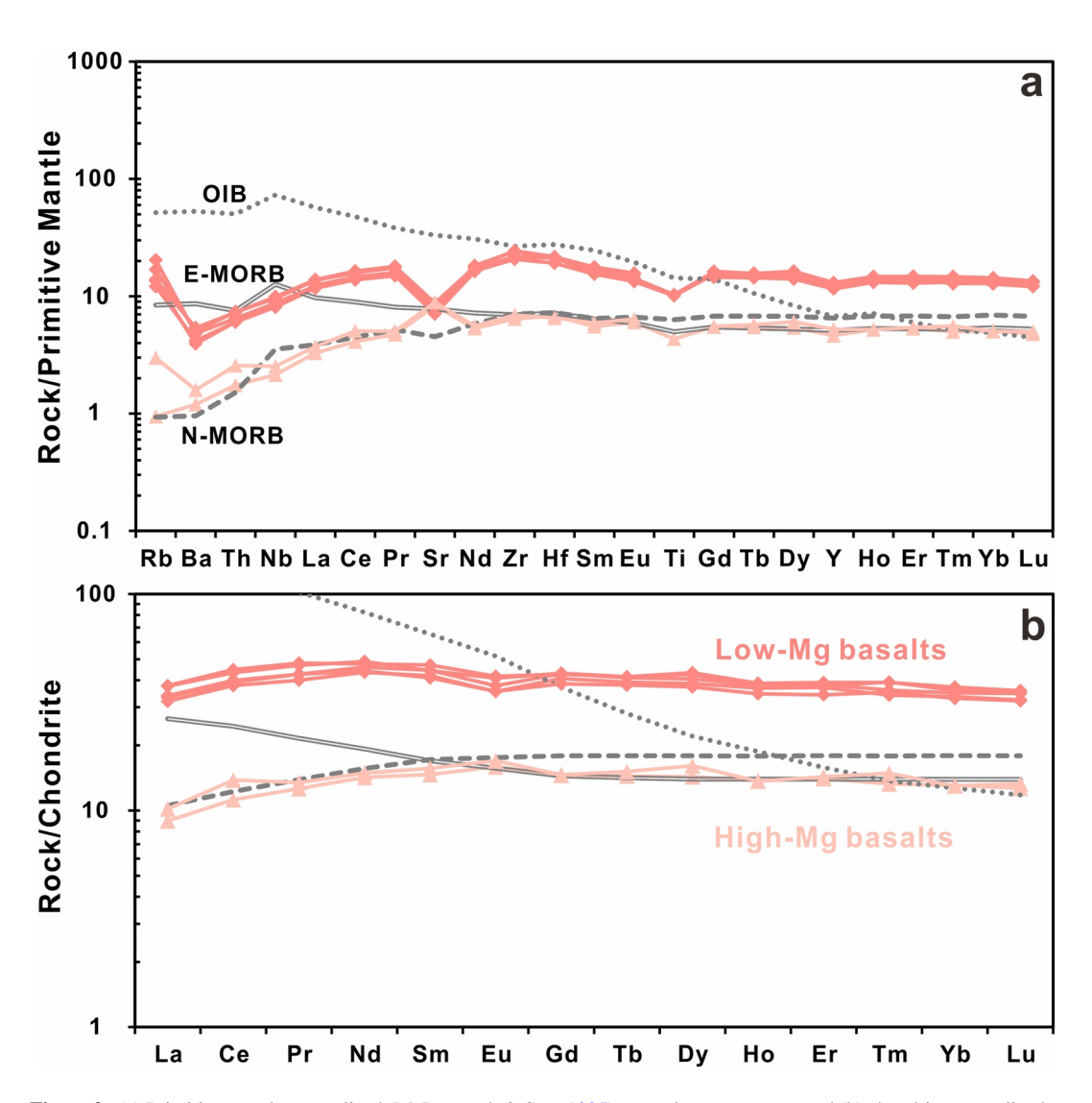


Figure 3. (a) Primitive mantle-normalized (McDonough & Sun, 1995) trace element patterns and (b) chondrite-normalized (Sun & McDonough, 1989) rare earth element patterns of the high-Mg and low-Mg basalts. N-MORB, E-MORB, and OIB data are from Sun and McDonough (1989).

software developed at the Ruhr-Universitaet Bochum. Calculation of the angles between crystallographic axes and the measured electron microprobe traverses in olivine allowed us to correct the strong anisotropic diffusion (e.g., Costa & Chakraborty, 2004).

5. Results

5.1. Whole-Rock Major and Trace Element Compositions

Based on major element compositions, the basalts can be classified into two groups, that is, high-Mg and low-Mg. The high-Mg group is relatively primitive and characterized by high Mg# (molar $100 \times \text{Mg/(Mg} + \text{Fe)}$) of ~ 66 . In contrast, the low-Mg group is compositionally more evolved and has slightly higher Na₂O, SiO₂, FeO^T, lower Al₂O₃, CaO, MgO contents, and low Mg# of ~ 47 (Table S1). These compositions are consistent with the primitive and evolved natures of their parental magmas, respectively. The chondrite-normalized rare earth element patterns of the high-Mg and low-Mg basalts are sub-parallel, with light rare earth elements slightly depleted relative to heavy rare earth elements, similar to that of the N-MORB (Figure 3). The abundances of rare earth elements in low-Mg basalts are relatively high compared with the high-Mg counterparts (Figure 3 and Figure S2 in Supporting Information S1). Consistently, the Eu/Eu* anomalies change from slightly positive in high-Mg basalts to negative in low-Mg basalts,

MA ET AL. 5 of 17

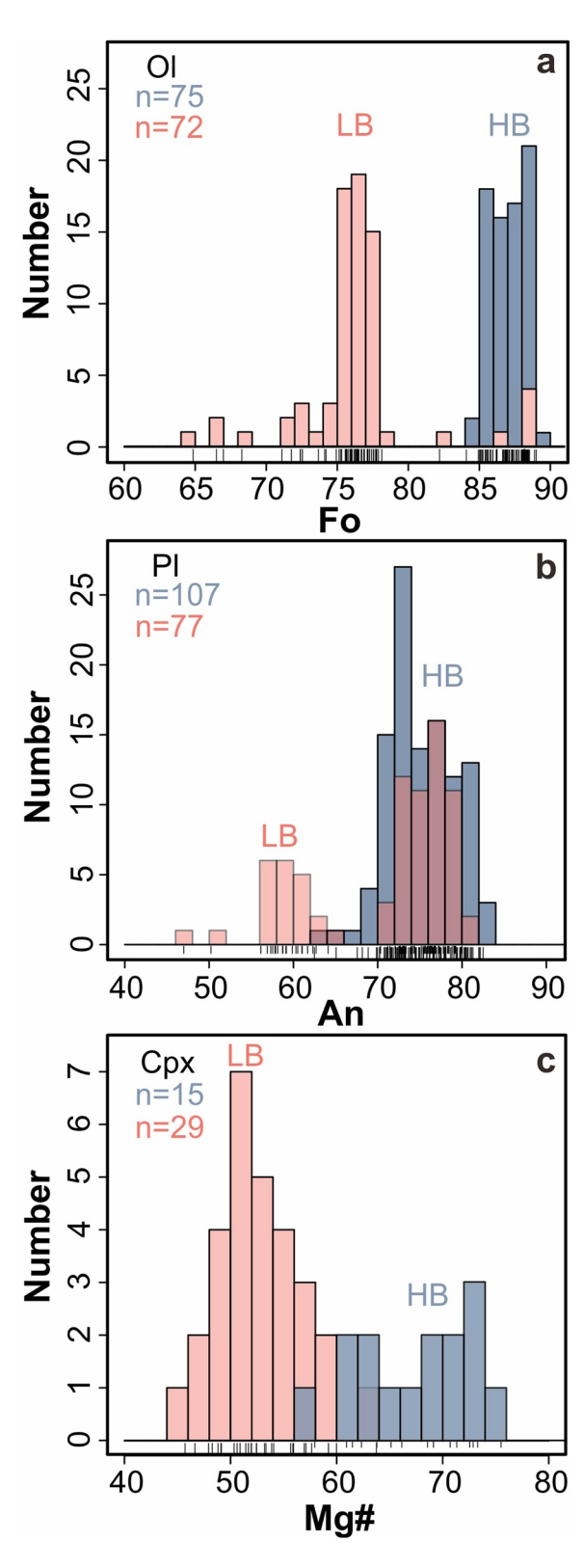


Figure 4. Compositional variations of olivine (Ol), plagioclase (Pl) and clinopyroxene (Cpx) in high-Mg and low-Mg basalts (HB and LB).

which implies plagioclase fractionation during evolution of the low-Mg basaltic melts (Figure S2b in Supporting Information S1).

5.2. Mineral Major Element Compositions

Olivine phenocrysts in the high-Mg basalts have weak compositional zoning with Fo (Mg/(Mg + Fe) \times 100) values ranging from 85 to 89 (Figure 2a, Table S2). Olivine crystallites in the matrix of the high-Mg basalts have Fo values of ~85. In contrast, olivine phenocrysts from the low-Mg basalts have Fo values ranging from 72 to 77 (Figure 4, Table S2). Normally zoned olivine grains in low-Mg basalts have Fo values of ~88 in cores and ~75 in rims (Figure 2e). From core to rim, the zoned olivine grains show a gradual decrease in MgO and NiO contents and a gradual increase in FeO and MnO contents, whereas CaO and Al₂O₃ contents remain constant within analytical error (Figure S3 in Supporting Information S1).

Plagioclase grains from the high-Mg basalts have An (Ca/(Ca + Na) \times 100) contents varying from \sim 63 to 82, whereas those from the low-Mg basalts have An contents varying from \sim 47 to 80 (Figure 4). In low-Mg basalts, normally zoned plagioclase grains have cores with An contents of \sim 77 and rims with An contents of \sim 57 (Figure 2f). Olivine and plagioclase glomerocrysts have compositions (Fo = 75–77, An = 57–62) similar to olivine and plagioclase phenocrysts in low-Mg basalts (Figure 2c). The Mg# of clinopyroxene crystallites varies from 60 to 75 in high-Mg basalts and from 46 to 63 in low-Mg basalts (Figure 4).

5.3. Crystallization Temperatures and Pressures of Olivine and Plagioclase

Olivine and plagioclase phenocrysts are <5 vol.% in high-Mg basalts and the Fe-Mg exchange coefficients between olivine phenocrysts (Fo = 87–89) and the whole-rock compositions of high-Mg basalts (as liquids) are 0.28-0.33, indicating that they are in equilibrium $(K_D(\text{Fe-Mg})^{\text{ol-liq}} = 0.30 \pm 0.03; \text{Roeder})$ & Emslie, 1970). Thus, whole-rock compositions can represent the melt compositions from which these olivine grains crystallized. Similarly, the An-Ab exchange coefficients between plagioclase phenocrysts (An = 76-80) and the whole-rock compositions of high-Mg basalts (as liquids) are restricted to 0.24 to 0.30, indicating that they are also in equilibrium (well within the range of $K_D(\text{An-Ab})^{\text{pl-liq}} = 0.27 \pm 0.11$, $T \ge 1,050$ °C; Putirka, 2008). Using the same method, olivine and plagioclase phenocrysts with no core-rim textures in low-Mg basalts are compositionally in equilibrium with their whole-rock compositions (as liquids). Moreover, low Ni/Co and Ni/Mn ratios of the high-Fo olivine grains in high-Mg basalts also indicate that they are phenocrysts crystallized from the melt, instead of mantle xenoliths (Figure S4 in Supporting Information S1; Wang et al., 2021). Therefore, plagioclase, olivine and whole-rock compositions of high-Mg and low-Mg basalts (as liquid compositions) can be used to calculate crystallization temperatures and pressures.

Using plagioclase-liquid thermobarometer of Putirka (2008), plagioclase phenocrysts in the high-Mg basaltic melts were crystallized at $\sim 10.7 \pm 2.5$ kbar and $\sim 1,300 \pm 36$ °C, and those in the low-Mg basaltic melts

MA ET AL. 6 of 17

21699356, 2024, 1, Downloaded from https://agupubs.onlinelibrary.wiley.com/doi/10.1029/2023JB027224 by University Of Alaska Fairbanks,

Figure 5. Calculated temperature and pressure results. (a) Crystallization temperatures of olivine calculated by olivine-liquid thermometer. Olivine-liquid thermometer results represent the average of the calculated results from Putirka (2008), see Table S3 for details. K_D represents the Fe-Mg exchange coefficient. (b) Crystallization temperatures and pressures calculated by plagioclase-liquid thermobarometer (Equations 24a and 26 are different thermometer equations from Putirka (2008)). Crystallization pressures obtained by petrological barometer given by Herzberg (2004) (H04) and Yang et al. (1996) (Yang96) are also shown in light gray bands. Liquidus line temperatures calculated from Rhyolite-MELTS (Gualda et al., 2012) are also plotted in red solid lines in (b). QFM-1 and 0.2 wt.% H₂O are used. Pl = plagioclase.

were crystallized at \sim 4.4 \pm 2.5 kbar and \sim 1,180 \pm 36°C (Figure 5, Table S3). Using olivine-liquid thermometers of Putirka (2008), olivine phenocrysts in high-Mg basaltic melts were crystallized at \sim 1,210 \pm 43°C, whereas those in low-Mg basaltic melts were crystallized at \sim 1,170 \pm 45°C (Figure 5, Table S3).

The credibility of plagioclase-liquid barometer is further supported by MELTS (Gualda et al., 2012), which shows that melts with compositions similar to the high-Mg basalts can crystallize plagioclase with An = 75 at 10 kbar and QFM-1, whereas melts with compositions similar to the low-Mg basalts can crystallize plagioclase with An = 61 at 4 kbar and QFM-1. The liquidus temperatures obtained by MELTS are 1,295–1,367°C at 8–13 kbar for the high-Mg basaltic melts and 1,182–1,235°C at 2–6 kbar for the low-Mg basaltic melts (Figure 5b), which roughly agree with those obtained by plagioclase-liquid thermobarometers. Given that the cores and rims of the normally zoned olivine and plagioclase in low-Mg basalts have compositions similar to those crystallized from high-Mg and low-Mg basaltic melts (Figure 2), we speculate that the olivine and plagioclase cores were crystallized at similar P-T conditions with those in high-Mg basalts and the olivine and plagioclase rims were crystallized at similar P-T conditions with those in low-Mg basalts.

For comparison, we also calculated the crystallization pressures of high-Mg and low-Mg basalts using petrological barometers as a reference because crystal-melt reactions are common at ultraslow-spreading ridges (Herzberg, 2004; Kelley & Barton, 2008; Yang et al., 1996). Results show that the high-Mg basaltic melts were crystallized at 9.2 ± 1.4 kbar and the low-Mg basaltic melts were crystallized at 4.1 ± 1.4 or 3.0 ± 1.0 kbar (Figure 5b).

6. Discussion

6.1. Deep Roots of the Magma Plumbing Systems Beneath the Ultraslow-Spreading SWIR

Overall, the crystallization depths of MOR basaltic melts in slower-spreading ridges are deeper than that of faster-spreading ridges (e.g., Grove et al., 1992; Herzberg, 2004; Wanless & Behn, 2017). The negative correlations between crystallization pressures and spreading rates could be due to variations in magma flux and advective heat (Michael & Cornell, 1998). Compared with faster-spreading ridges, slower-spreading ridges have lower magma supply, more transform faults, thinner crust, and deeper circulation of seawater, which could contribute to the deeper crystallization depth of magmas in slower-spreading ridges (e.g., Herzberg, 2004; Michael & Cornell, 1998; Schlindwein & Schmid, 2016; Shen & Forsyth, 1995; White et al., 2001).

Due to potential gravitational subsidence, olivine crystals erupted may capture only a fraction of the entire depth range of the magma plumbing systems (Bennett et al., 2019; Maclennan, 2017) as they equilibrate relatively

MA ET AL. 7 of 17

rapidly with the melt, even though their dissolution is slow. In contrast, plagioclase dissolves relatively rapidly and equilibrates slowly via diffusion (e.g., Kvassnes & Grove, 2008). Hence plagioclase phenocrysts in MORB frequently preserve complex zoning and have rounded outlines, whereas olivine is rarely zoned and often has euhedral morphology. Thus, plagioclase can record multi-stage processes and deeper crystallization depth than olivine (Figure 2a; Bennett et al., 2019). The calculated crystallization depth of the high-Ca plagioclase in the high-Mg basalts using plagioclase-liquid thermobarometers and MELTS simulations is $\sim 10.7 \pm 2.5$ kbar, corresponding to a depth of $\sim 32 \pm 7.8$ km using an average density of 3.3 g cm⁻³. This assumes that serpentinization of the mantle is relatively shallow given that much of the mantle sampled in this region is highly weathered but otherwise fresh peridotite mylonite. These mylonites are associated with the emplacement of the mantle to the seafloor in the region and have undergone only minor static serpentinization. Such fine-grained mylonites are relatively impermeable to hydrothermal circulation in such a static shallow mantle environment following emplacement.

Up to present the deepest crystallization depth reported petrographically is for the ultraslow-spreading Gakkel Ridge based on olivine and plagioclase-hosted melt inclusion volatile contents ($\leq \sim 16.4$ km; Bennett et al., 2019), whereas it is ~ 20 km in depth derived from seismicity data measured from $\sim 12^{\circ}$ to 14° E on a western SWIR amagmatic segment (Grevemeyer et al., 2019; Schlindwein & Schmid, 2016). However, based on the seafloor morphology, the 12° to 14° E segment has existed for at least 10 Ma, while the small spreading center where our sample was dredged was only ~ 0.7 Ma old. Thus, it is likely that the lithosphere when the Dr. 27 basalts erupted was considerably thicker.

Our constraints on the depth to the top of the melting column at the $45^{\circ}E$ ultraslow-spreading ridge segment are similar or deeper to the ~ 25 km estimated by Shaw et al. (2010) for the $85^{\circ}E$ segment of the ultraslow-spreading Gakkel ridge, and deeper than other estimates of the ultraslow-spreading ridges (~ 20 km; White et al., 2001). Although, the standard error is large for our data, this is likely similar to that for the Gakkel Ridge data. Thus, the relative depth obtained by us is considerably deeper, and is the deepest reported so far. Basaltic melts generated by decompressional partial melting of the asthenosphere are expected to start to crystallize near the base of the lithospheric mantle as melt mass begins to shrink due to conductive heat loss. However, if accurate, a depth of 32 km would seem to imply that crystallization began in the shallow asthenosphere. However, there is considerable debate about the nature of the asthenosphere-lithosphere boundary. Our data then imply that there is likely a considerably different thermal structure beneath a long-lived amagmatic ultraslow-spreading oblique ridge segment than for an orthogonal spreading magmatic segment in the same environment, consistent with the expected effect on mantle upwelling rate and conductive heat loss (Dick et al., 2003).

6.2. Deep Axial Magma Chambers of the Ultraslow-Spreading SWIR

The existence and depth of AMCs have been demonstrated by seismic tomography. Their depths commonly do not exceed 4 km and seem to be negatively correlated with spreading rates (Chen, 2004; Rubin & Sinton, 2007). AMCs have been frequently detected at fast- and intermediate-spreading ridges with thick crust and abundant melt supply (e.g., Canales et al., 2006; Detrick et al., 1987). In contrast, very few AMCs have been reported for slow- and ultraslow-spreading ridges (e.g., Jian et al., 2017; Singh et al., 2006), which indicates that ridges with low melt supply and thin or absent oceanic crust are unfavorable for the formation of AMCs (Phipps Morgan & Chen, 1993). Deep AMCs (~4–9 km) detected by seismic data beneath ultraslow-spreading ridges are highly localized compared to the thin elongated examples at faster-spreading ridges. This is consistent with three-dimensional focusing of mantle and melt beneath slow spreading ridges (e.g., Whitehead et al., 1984).

Due to their similar trace element and REE distribution patterns, we suggest that the low-Mg basaltic melts are evolutionary products of the high-Mg counterparts (Figure 3). The negative Eu/Eu* anomalies and depleted Sr contents of the low-Mg basalts imply plagioclase fractionation. As shown by previous magma chamber models for the differentiation of ridge basalts, fractional crystallization alone cannot reproduce the major and trace element distribution patterns of all MORBs (e.g., Coogan & O'Hara, 2015; O'hara, 1977; O'Neill & Jenner, 2012; Langmuir, 1989; Lissenberg & MacLeod, 2016). These models all appeal to the existence of an AMC as a necessary condition to explain MORB genesis. Prima facie evidence is the requirement for magma mixing to explain normal and reverse zoning in phenocryst populations in a single lava, and to explain the evidence of cross-contamination in these melts (e.g., Anderson, 1976) as we have shown here for the Dr. 27 lavas (Figure 2). Consequently, plagioclase and olivine glomerocrysts in highly phyric MORBs are commonly interpreted as

MA ET AL. 8 of 17

representing crystal mushes from a melt storage region in the crust and evidence for magma mixing (e.g., Dick & Bryan, 1978; Dungan et al., 1978; Lissenberg et al., 2019; Rhodes et al., 1979). Given that the unzoned plagioclase phenocrysts and plagioclase glomerocrysts in the low-Mg basalts have similar compositions and were both crystallized at $\sim 13 \pm 7.8$ km, the magma chamber or melt storage region would be located at similar or greater depth (Figure 5, Table S3). This depth appears deeper than the majority of the AMCs reported underneath global ridges so far, as previously recognized for slower-spreading ridges (Chen, 2004; Rubin & Sinton, 2007; Shaw et al., 2010).

6.3. Olivine Residence Time and Magma Ascent Rates of the Ultraslow-Spreading SWIR

Diffusion modeling of Fe-Mg, Ni, and Mn in compositionally zoned olivine phenocrysts was carried out to calculate olivine residence time (Methods and uncertainties in Supporting Information S1). This time represents the period from growth of the olivine rims in low-Mg basaltic melts to eruption on the seafloor. The zoning of olivine (CaO and Al_2O_3 contents remain constant from core to rim) is mainly induced by diffusion instead of growth (see Text S2 for details in Supporting Information S1). For diffusion modeling, a step function is assumed for the initial profile and temperatures of 1,190 and 1,170°C are used (Figure 6). Oxygen fugacity is determined through V partition coefficients between olivine and silicate melts (see Text S1 text for details in Supporting Information S1).

Modeling results show that the olivine residence time varies from 2 weeks to 3 months, which is the time for olivine crystals to grow in the ~13 km deep AMC and then ascend to the seafloor (Figures 6 and 7). This timescale is indistinguishable with the olivine residence time at fast- and slow-spreading ridges (Costa et al., 2020; Danyushevsky et al., 2002; Hartley et al., 2016; Mutch et al., 2019; Nabelek & Langmuir, 1986; Pan & Batiza, 2002). In general, studies of MORBs based on zoned olivine and plagioclase phenocrysts and xenocrysts show that their residence time is within one day to a few years (Figure 7; Costa et al., 2010, 2020; Danyushevsky et al., 2002; Hartley et al., 2016; Humler & Whitechurch, 1988; Moore et al., 2014; Nabelek & Langmuir, 1986; Pan & Batiza, 2002; Zellmer et al., 2011, 2012). A data compilation shows that olivine residence time may not have essential correlations with the spreading rates (Figure 7). Likewise, the differences in mineralogy and residence time between robust and non-robust East Pacific Rise segments are not significant (Pan & Batiza, 2002). However, Zellmer et al. (2012) reported that the residence time of plagioclase obtained by Mg and Sr diffusion, although with a large time range, are on average systematically longer at slower-spreading ridges and off-axis ridges (Figure 7). The variable residence time of plagioclase and its complex textures seem to be related to the differences in the dynamics of late-stage, pre-eruptive magma storage and ascent processes in different ridges (Zellmer et al., 2012).

The magma ascent rates of MORBs are commonly determined by vesicle size distribution (VSD) and volatile (CO₂ and H₂O) contents in matrix glasses (Chavrit et al., 2012; Gardner et al., 2016; Soule et al., 2012). The calculated magma ascent rates of global MORBs range from ~0.1 to 1 m/s (Chavrit et al., 2012; Gardner et al., 2016; Soule et al., 2012), and are positively correlated with the spreading rates (Chavrit et al., 2012). However, magma ascent rates calculated based on VSD and volatile contents of the basaltic glasses are usually constrained to depths of <~7 km (e.g., Chavrit et al., 2012; Wanless & Behn, 2017), which predominantly represents magma ascent rates at shallow depths prior to eruptions. Magma usually rises faster near the surface than at depth, consistent with the upward acceleration or a temporary stall at depth (e.g., Neave & Maclennan, 2020). For example, the decoupling of multi-element (e.g., Fe-Mg, Mn, Ni, and Ca) and water diffusion time in olivine xenocrysts from Pupuke Maar volcano suggested that the water diffusion profiles may record shallow degassing of magmas prior to eruption, whereas the major and minor element (e.g., Fe-Mg, Mn, Ni, and Ca) diffusions of minerals reveal possible ascent rates after entrainment in the deep lithosphere (Brenna et al., 2018). Diffusion chronometers combined with mineral barometers, on the other hand, can be applied to obtain average magma ascent rates from a greater depth compared to VSD method (e.g., Costa et al., 2020; Mutch et al., 2019). For example, olivine diffusion chronometer and clinopyroxene-liquid barometer of wehrlite nodules from the Icelandic Borgarhraun lava showed that magma ascent rate from near-Moho storage (~24 km deep) to the surface was ~0.02–0.1 m/s (Mutch et al., 2019). Yet for the ultraslow-spreading ridges where the crust is very thin or missing, little is known about how rapid melt can move through the lithosphere.

According to the olivine diffusion chronometers and different barometers, the mean trans-lithospheric ascent rate of the Dr. 27 melts from a depth of \sim 13 km to the seafloor is at least 0.002–0.01 m/s, which is about one to two

MA ET AL. 9 of 17

21699356, 2024, 1, Downloaded from https://agupubts.onlinelibrary.wiley.com/doi/10.10292023JB027224 by University Of Alaska Fairbanks, Wiley Online Library on [30/12/2024]. See the Terms and Conditions (https://onlinelibrary.wiley.com/doi/10.10292023JB027224 by University Of Alaska Fairbanks, Wiley Online Library on [30/12/2024]. See the Terms and Conditions (https://onlinelibrary.wiley.com/doi/10.10292023JB027224 by University Of Alaska Fairbanks, Wiley Online Library on [30/12/2024]. See the Terms and Conditions (https://onlinelibrary.wiley.com/doi/10.10292023JB027224 by University Of Alaska Fairbanks, Wiley Online Library on [30/12/2024]. See the Terms and Conditions (https://onlinelibrary.wiley.com/doi/10.10292023JB027224 by University Of Alaska Fairbanks, Wiley Online Library on [30/12/2024]. See the Terms and Conditions (https://onlinelibrary.wiley.com/doi/10.10292023JB027224 by University Of Alaska Fairbanks, Wiley Online Library on [30/12/2024]. See the Terms and Conditions (https://onlinelibrary.wiley.com/doi/10.10292023JB027224 by University Of Alaska Fairbanks, Wiley Online Library on [30/12/2024]. See the Terms and Conditions (https://onlinelibrary.wiley.com/doi/10.10292023JB027224 by University Of Alaska Fairbanks, Wiley Online Library on [30/12/2024]. See the Terms and Conditions (https://onlinelibrary.wiley.com/doi/10.10292023JB027224 by University Online Library.wiley.com/doi/10.10292023JB02724 by University Online Library.wiley.

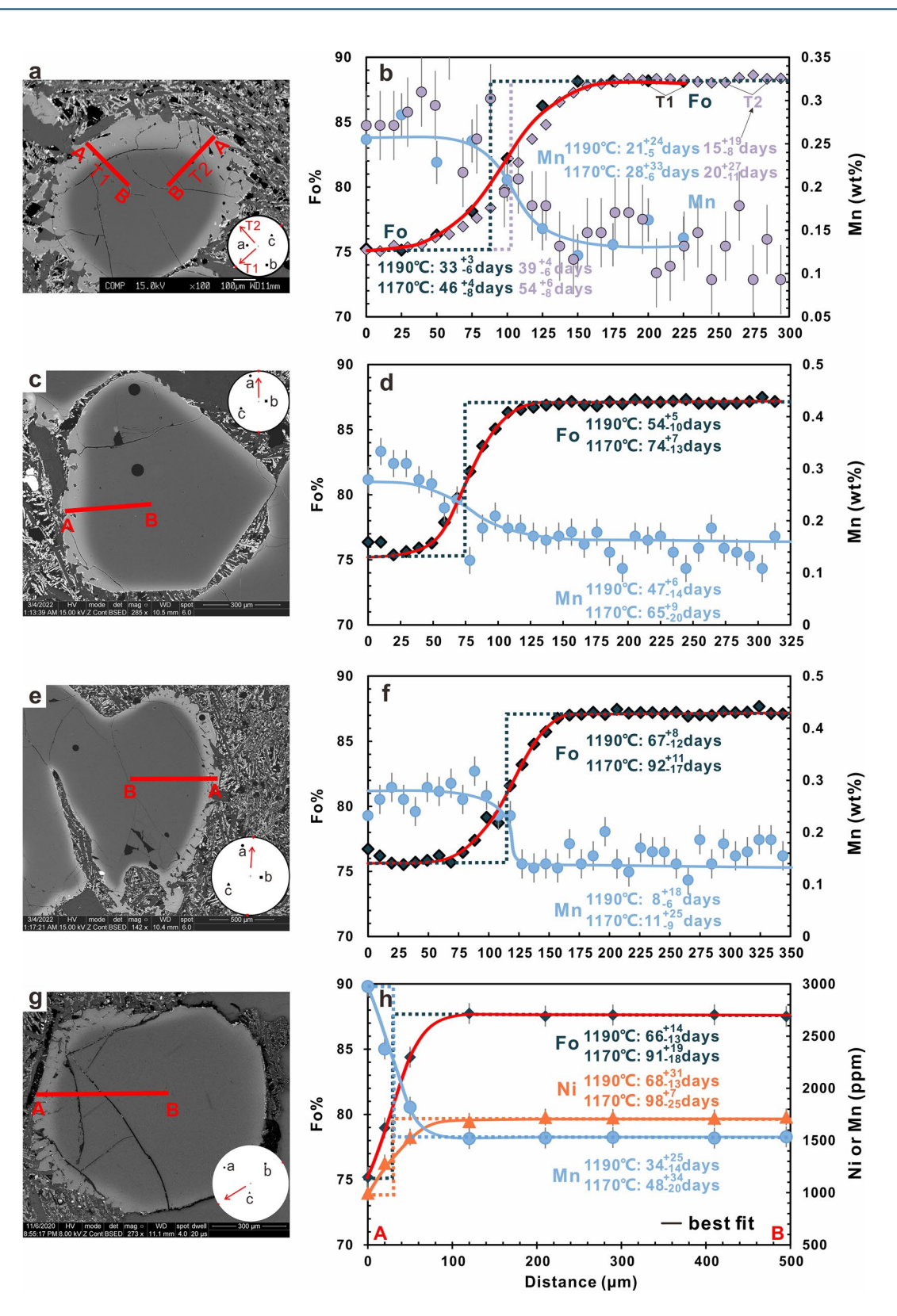


Figure 6. Representative diagrams showing the zoning of olivine crystals and corresponding diffusion timescales. The rim-to-core compositional profile is drawn on the olivine BSE images (red line, a, c, e, g). Dashed lines represent the initial compositional distribution profile. The stereographic plot in (a), (c), (e), and (g) indicates the angular relations between the (a)–(c) crystallographic axes in olivine and the directions of the measured rim-to-core traverses. The uncertainty on the diffusion timescales is based on the discrepancy from the DIPRA model (Girona & Costa, 2013). The Ni and Mn contents in (h) are from our unpublished data.

MA ET AL. 10 of 17

21699356, 2024, 1, Downloaded from https://agupubs.onlinelibrary.wiley.com/doi/10.1029/2023JB027224 by University Of Alaska Fairbanks, Wiley Online Library on [30/12/2024]. See the Terms

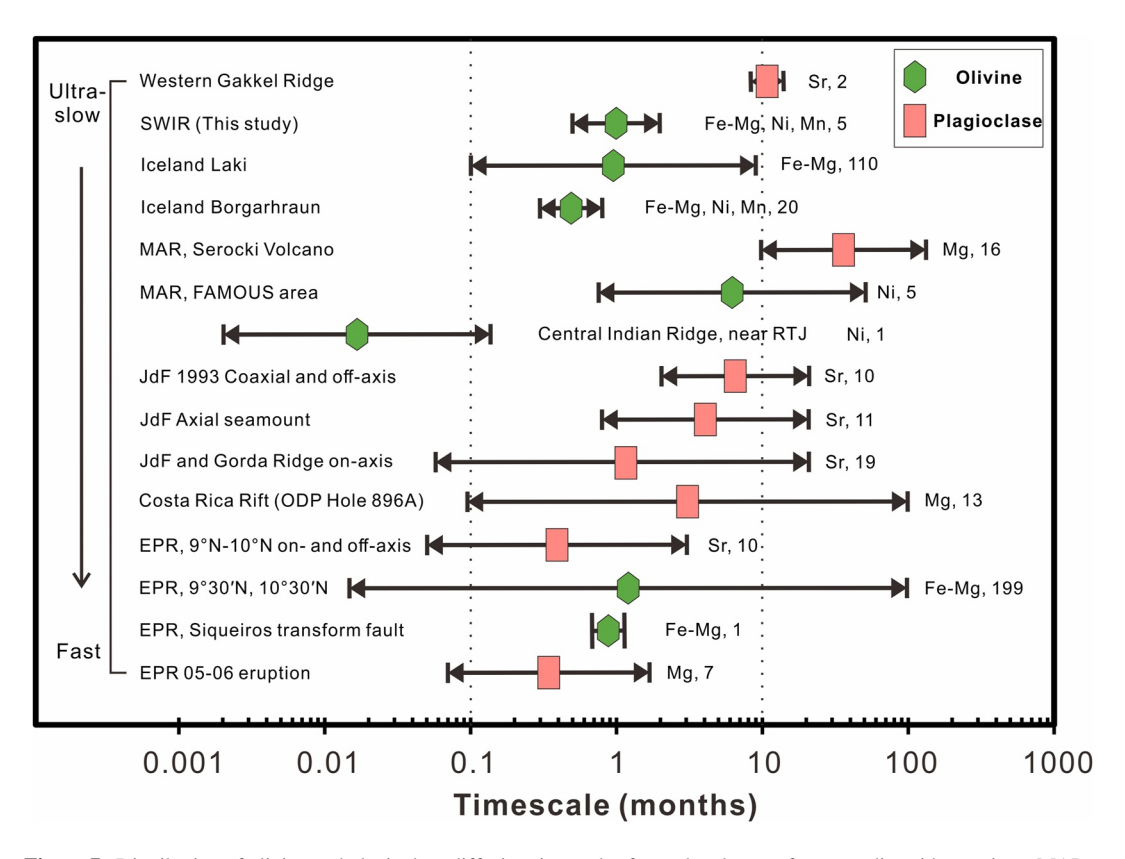


Figure 7. Distribution of olivine and plagioclase diffusion timescales from ultraslow- to fast-spreading ridge settings. MAR is Mid-Atlantic Ridge, RTJ is Rodriguez triple junction, JdF is Juan de Fuca Ridge, EPR is East Pacific Rise. The elements and number of profiles modeled for deriving timescales are also shown. References are as follows: Costa et al. (2010), Danyushevsky et al. (2002), Hartley et al. (2016), Humler and Whitechurch (1988), Moore et al. (2014), Mutch et al. (2019), Nabelek and Langmuir (1986) Pan and Batiza (2002), Zellmer et al. (2011, 2012).

orders of magnitude slower than other ridges (Figure 8). The dendritic morphology (high undercooling) of olivine rims likely occurs during the ascent of olivine from the AMC. Thus, the hypothesis that the magma residence time is significantly shorter than magma ascent time is valid. We have calculated that it would take \sim 30–300 min to grow such olivine rims, which is negligible considering the diffusion timescales (see Text S1 for details in Supporting Information S1).

Although the methods for obtaining magma ascent rates are different, it is conspicuous that there is a positive correlation between magma ascent rates and spreading rates of the ridges (Figure 8; Chavrit et al., 2012). The magma ascent rates of the 45°E SWIR in this study are about an order of magnitude slower than those of the ultraslow-spreading Icelandic Borgarhraun lavas rising from a depth of ~24 km to the surface (Figure 8; Mutch et al., 2019; Neave & Maclennan, 2020). Given that the spreading rates of the two are close, the faster ascent rate of the Iceland MOR have been suggested to be affected by mantle plume activities (Poore et al., 2011; Putirka, 2005). The magma ascent rate we calculated is more than an order of magnitude slower than those obtained by VSD and volatile methods for numerous samples along the eastern half of SWIR (Chavrit et al., 2012). The difference then likely reflects an increasing speed of magma ascent from far greater depth (13 vs. 7 km) to the seafloor.

In comparison, the ascent rates of arc magmas have a larger range of variation than the global ridges (Figure 8) due largely to their high volatile contents compared to relatively anhydrous MOR basaltic melts. In arc settings, mass eruption rate of magmas were considered to correlate positively with ascent rates (e.g., Barth et al., 2019; Ferguson et al., 2016; Newcombe et al., 2020), such as the 1974 eruption of the Volcano de Fuego (\log_{10} MER = 6.5, ~10 m/s) and the two moderately explosive eruptions of the Cerro Negro in 1992 (\log_{10} MER = 5.0, ~0.2 m/s median) and 1995 (\log_{10} MER = 4.1, ~0.03 m/s median) (Figure 8; Barth et al., 2019; Lloyd et al., 2014). Kimberlites and alkaline basalts, which are commonly volatile-rich due to their formation by low-degree partial melting of the mantle rocks, also tend to have high magma ascent rates (mostly >1–30 m/s) (Figure 8; e.g., Demouchy et al., 2006; Peslier et al., 2008, 2015).

MA ET AL. 11 of 17

, 2024, 1, Downloaded from https://agupubs.onlinelibrary.wiley.com/doi/10.1029/2023JB027224 by University Of Alaska Fairbanks, Wiley Online Library on [30/12/2024]. See the Terms and Conditions

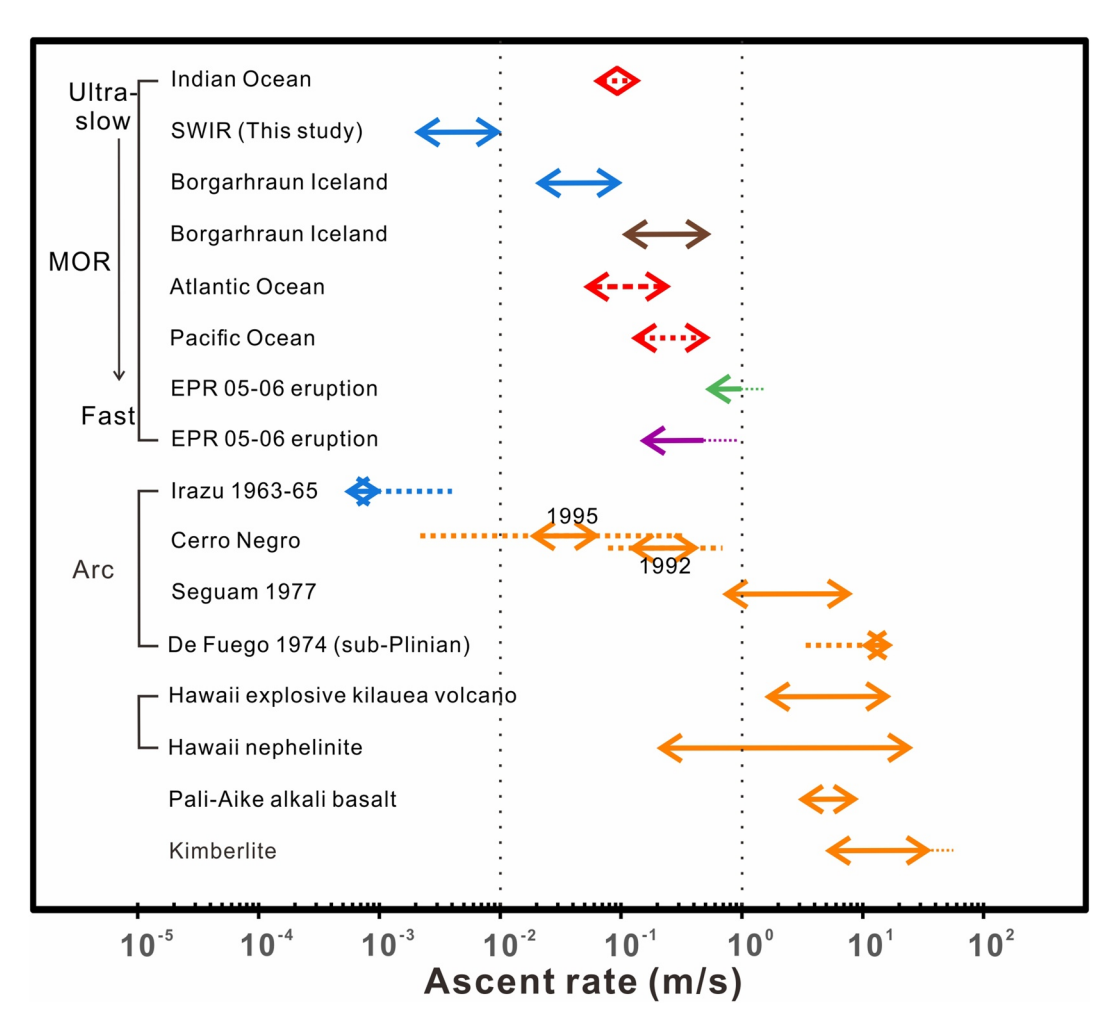


Figure 8. Magma ascent rates and literature comparison with other magma in different tectonic settings. The different colors of the ascent rate represent different research methods. The red represents vesicle size distribution and volatile measurements (CO_2 and H_2O), the blue represents the numerical modeling of Fe-Mg, Ni, and Mn elements in olivine, the green is decompression experiment and CO_2 modeling, the purple represents modeling of diffusion-controlled bubble growth, the brown represents modeling the dissolution of clinopyroxene crystals, the orange represents the modeling of diffusive volatile loss, mainly water diffusion, from melt embayments, olivine-hosted melt inclusions or olivine phenocryst to constrain the decompression rate. References are as follows: Chavrit et al. (2012), Gardner et al. (2016), Soule et al. (2012), Mutch et al. (2019), Neave and Maclennan (2020), Ruprecht and Plank (2013), Newcombe et al. (2020), Barth et al. (2019), Lloyd et al. (2014), Peslier et al. (2015), Demouchy et al. (2006).

6.4. Ascent Processes of the Deep-Rooted Magma of the 45°E SWIR

The magma flux is relatively abundant at fast- and intermediate-spreading ridges (e.g., Canales et al., 2006; Detrick et al., 1987; Phipps Morgan & Chen, 1993), whereas at ultraslow-spreading ridges it is low and commonly flows along the lithosphere-asthenosphere boundary (LAB) (e.g., Cannat et al., 2008; Jian et al., 2017; Montési et al., 2011; Standish et al., 2008). The thermal structure of the ridge axis exerts a primary control on the axial morphology, which is a function of spreading rate and magma supply (Ito & Behn, 2008; Phipps Morgan & Chen, 1993). The formation and distribution of axial melt lenses or AMCs are more or less related to the spreading rates (e.g., Chen, 2004; Liu & Buck, 2023; Rubin & Sinton, 2007). In the case of the ultraslow-spreading SWIR, high-Mg basaltic melts carrying high-Mg olivine and high-Ca plagioclase phenocrysts may ascend directly to the seafloor from a depth of as much as \sim 32 \pm 7.8 km, or they can likely undergo differentiation in a melt storage region at \sim 13 \pm 7.8 km where they evolved to low-Mg basaltic magmas before being erupted on the seafloor (Figure 9).

Our study shows that the magma plumbing system and melt storage region at the 45°E segment lie deep in the mantle, as the crust at this location at a small young ridge segment lying in an enormous region where the mantle

MA ET AL. 12 of 17

21699356, 2024, 1, Downloaded from https://agupubs.onlinelibrary.wiley.com/doi/10.1029/2023JB027224 by University Of Alaska Fairbanks, Wiley Online Library on [30/12/2024]. See the Terms

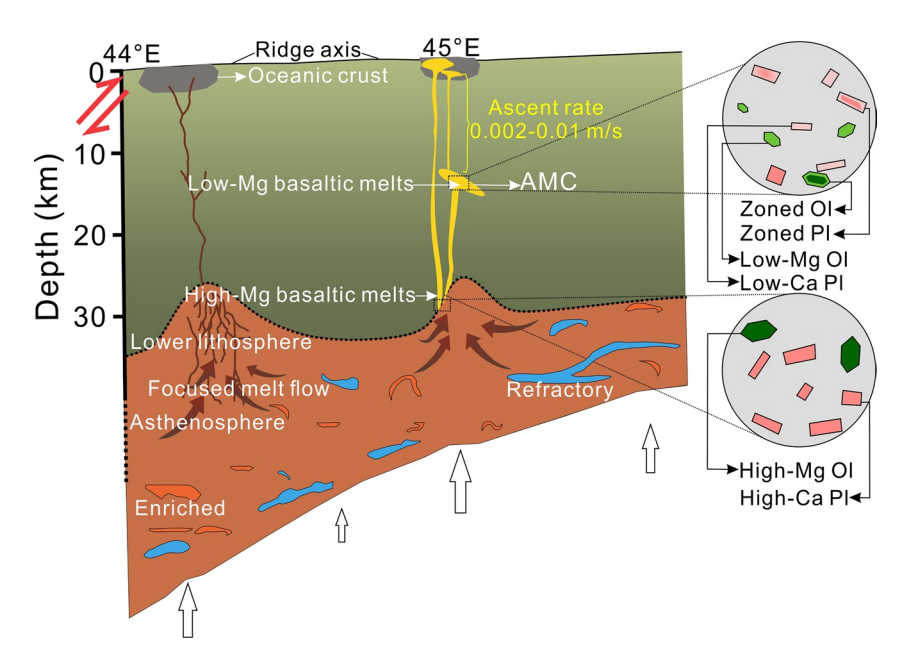


Figure 9. Schematic along-axis cross section showing our tectono-magmatic MORB generation model on the Southwest Indian Ridge (\sim 45°E). A high-Mg basaltic composition ascended directly to the seafloor from a depth of \sim 32 \pm 7.8 km, whereas the composition of low-Mg basalt lingered at \sim 13 \pm 7.8 km deep axial magma chamber. Ol, olivine, Pl, plagioclase, AMC, axial magma chamber.

is exposed directly to the seafloor is almost certainly thin. This depth is close to the LAB, or even depending on how the LAB is defined, into the shallow asthenosphere, which complements previous perception that the spreading rates could be negatively correlated with the crystallization depths of the MOR basaltic melts (Figure 9; e.g., Chen, 2004; Grove et al., 1992; Herzberg, 2004; Rubin & Sinton, 2007; Wanless & Behn, 2017). The mean trans-lithospheric magma ascent rate from a depth of ~13 km to the seafloor at 45°E SWIR is also the slowest among global ridge systems reported so far (Figure 8). The deep-rooted plumbing system of the SWIR likely correlates with a cold oceanic lithosphere due to enhanced conductive heat loss induced by extensive circulation of seawater, low melt supply and slow spreading rate.

7. Conclusions

We have elucidated the magmatic ascent processes of the 45°E ultraslow-spreading SWIR by new petrographic evidence, in particular using normally zoned olivine and plagioclase grains. The following conclusions are made:

- 1. The roots of the magma plumbing system are close to the base of the lithospheric mantle beneath the 45°E SWIR, which implies that partial crystallization may have occurred deep in the lithospheric mantle at least at ultraslow-spreading ridges.
- AMCs may have existed at a deeper depth beneath ultraslow-spreading ridges, as previously recognized for slower-spreading ridges.
- 3. Olivine grains may have resided in the magma for tens of days before being erupted on the seafloor. The magma ascent rate of the 45°E SWIR could be the slowest among global MORs reported so far, which indicates that spreading rates may have fundamental controls on the dynamics of MOR magma plumbing systems.

Data Availability Statement

The data in this manuscript (Tables S1–S3) are available in the Figshare database via https://doi.org/10.6084/m9.figshare.24347419.v2 (Ma et al., 2023).

MA ET AL. 13 of 17

Acknowledgments

We thank Prof. Mark Dekkers and Prof. Fang-Zhen Teng for their efficient editorial handling. Two anonymous reviewers are thanked for their constructive comments and efficient reviewing work. The authors express appreciation for the cruise TN365. This study is financially supported by the National Science Foundation of China (Grant 42272051), and by travel funds and housing costs to HJBD provided by Peking University and the Institute of Geology and Geophysics, CAS.

References

- Anderson, A. T. (1976). Magma mixing: Petrological process and volcanological tool. *Journal of Volcanology and Geothermal Research*, 1, 3–33. https://doi.org/10.1016/0377-0273(76)90016-0
- Barth, A., Newcombe, M., Plank, T., Gonnermann, H., Hajimirza, S., Soto, G. J., et al. (2019). Magma decompression rate correlates with explosivity at basaltic volcanoes—Constraints from water diffusion in olivine. *Journal of Volcanology and Geothermal Research*, 387, 106664. https://doi.org/10.1016/j.jvolgeores.2019.106664
- Bennett, E. N., Jenner, F. E., Millet, M. A., Cashman, K. V., & Lissenberg, C. J. (2019). Deep roots for mid-ocean-ridge volcanoes revealed by plagioclase-hosted melt inclusions. *Nature*, 572(7768), 235–239. https://doi.org/10.1038/s41586-019-1448-0
- Bown, J. W., & White, R. S. (1994). Variation with spreading rate of oceanic crustal thickness and geochemistry. *Earth and Planetary Science Letters*, 121(3–4), 435–439. https://doi.org/10.1016/0012-821x(94)90082-5
- Brenna, M., Cronin, S. J., Smith, I. E. M., Tollan, P. M. E., Scott, J. M., Prior, D. J., et al. (2018). Olivine xenocryst diffusion reveals rapid monogenetic basaltic magma ascent following complex storage at Pupuke Maar, Auckland Volcanic Field, New Zealand. Earth and Planetary Science Letters, 499, 13–22. https://doi.org/10.1016/j.epsl.2018.07.015
- Canales, J. P., Singh, S. C., Detrick, R. S., Carbotte, S. M., Harding, A., Kent, G. M., et al. (2006). Seismic evidence for variations in axial magma chamber properties along the southern Juan de Fuca Ridge. Earth and Planetary Science Letters, 246(3–4), 353–366. https://doi.org/10.1016/j.epsl 2006.04.032
- Cannat, M., Sauter, D., Bezos, A., Meyzen, C., Humler, E., & Le Rigoleur, M. (2008). Spreading rate, spreading obliquity, and melt supply at the ultraslow spreading Southwest Indian Ridge. *Geochemistry, Geophysics, Geosystems*, 9(4), 140. https://doi.org/10.1029/2007gc001676
- Cannat, M., Sauter, D., Mendel, V., & Escartín, J. (2006). Large offset normal faults, ridge obliquity, and the distribution of volcanism at a melt-poor ultra-slow spreading ridge. In *Paper presented at AGU fall meeting abstracts*.
- Cannat, M., Sauter, D., Mendel, V., Ruellan, E., Okino, K., Escartin, J., et al. (2006). Modes of seafloor generation at a melt-poor ultraslow-spreading ridge. *Geology*, 34(7), 605–608. https://doi.org/10.1130/g22486.1
- Carbotte, S. M., Marjanović, M., Carton, H., Mutter, J. C., Canales, J. P., Nedimović, M. R., et al. (2013). Fine-scale segmentation of the crustal magma reservoir beneath the East Pacific Rise. *Nature Geoscience*, 6(10), 866–870. https://doi.org/10.1038/ngeo1933
- Chavrit, D., Humler, E., Morizet, Y., & Laporte, D. (2012). Influence of magma ascent rate on carbon dioxide degassing at oceanic ridges: Message in a bubble. Earth and Planetary Science Letters, 357–358, 376–385. https://doi.org/10.1016/j.epsl.2012.09.042
- Chen, Y. J. (2004). Modeling the thermal state of the oceanic crust. In Washington DC American geophysical union geophysical monograph
- series (Vol. 148, pp. 95–110). Cochran, J. R., Kurras, G. J., Edwards, M. H., & Coakley, B. J. (2003). The Gakkel Ridge: Bathymetry, gravity anomalies, and crustal accretion
- at extremely slow spreading rates. *Journal of Geophysical Research*, 108(B2), 2116. https://doi.org/10.1029/2002jb001830
- Colman, A., Sinton, J. M., & Wanless, V. D. (2015). Constraints from melt inclusions on depths of magma residence at intermediate magma supply along the Galápagos Spreading Center. Earth and Planetary Science Letters, 412, 122–131. https://doi.org/10.1016/j.epsl.2014.12.007
- Coogan, L. A., & O'Hara, M. J. (2015). MORB differentiation: In situ crystallization in replenished-tapped magma chambers. Geochimica et Cosmochimica Acta, 158, 147–161. https://doi.org/10.1016/j.gca.2015.03.010
- Costa, F., & Chakraborty, S. (2004). Decadal time gaps between mafic intrusion and silicic eruption obtained from chemical zoning patterns in olivine. Earth and Planetary Science Letters, 227(3–4), 517–530. https://doi.org/10.1016/j.epsl.2004.08.011
- Costa, F., Coogan, L. A., & Chakraborty, S. (2010). The time scales of magma mixing and mingling involving primitive melts and melt–mush interaction at mid-ocean ridges. Contributions to Mineralogy and Petrology, 159(3), 371–387. https://doi.org/10.1007/s00410-009-0432-3
- Costa, F., Shea, T., & Ubide, T. (2020). Diffusion chronometry and the timescales of magmatic processes. *Nature Reviews Earth & Environment*, 1(4), 201–214. https://doi.org/10.1038/s43017-020-0038-x
- Danyushevsky, L. V., Sokolov, S., & Falloon, T. J. (2002). Melt inclusions in olivine phenocrysts: Using diffusive re-equilibration to determine the cooling history of a crystal, with implications for the origin of olivine-phyric volcanic rocks. *Journal of Petrology*, 43(9), 1651–1671. https://doi.org/10.1093/petrology/43.9.1651
- Demouchy, S., Jacobsen, S. D., Gaillard, F., & Stern, C. R. (2006). Rapid magma ascent recorded by water diffusion profiles in mantle olivine. *Geology*, 34(6), 429. https://doi.org/10.1130/g22386.1
- Detrick, R., Buhl, P., Vera, E., Mutter, J., Orcutt, J., Madsen, J., & Brocher, T. (1987). Multi-channel seismic imaging of a crustal magma chamber along the East Pacific Rise. *Nature*, 326(6108), 35–41. https://doi.org/10.1038/326035a0
- Dick, H. J. B., & Bryan, W. B. (1978). Variation of basalt phenocryst mineralogy and rock compositions in DSDP Hole 396B. In *Initial reports* of the deep sea drilling Project XLVI (pp. 215–225).
- Dick, H. J. B., Lin, J., & Schouten, H. (2003). An ultraslow-spreading class of ocean ridge. *Nature*, 426(6965), 405–412. https://doi.org/10.1038/nature02128
- Dick, H. J. B., & Zhou, H. (2015). Ocean rises are products of variable mantle composition, temperature and focused melting. *Nature Geoscience*, 8(1), 68–74. https://doi.org/10.1038/ngeo2318
- Dungan, M. A., Long, P. E., & Rhodes, J. M. (1978). The petrography, mineral chemistry, and one-atmosphere phase relations of basalt from Site 395. In W. G. M. A. P. D. Rabinowitz (Ed.), *Initial reports of the deep sea drilling Project* (pp. 461–478). US Government Printing Office.
- Ferguson, D. J., Gonnermann, H. M., Ruprecht, P., Plank, T., Hauri, E. H., Houghton, B. F., & Swanson, D. A. (2016). Magma decompression rates during explosive eruptions of Kīlauea volcano, Hawaii, recorded by melt embayments. *Bulletin of Volcanology*, 78(10), 71. https://doi.org/10.1007/s00445-016-1064-x
- Gardner, J. E., Jackson, B. A., Gonnermann, H., & Soule, S. A. (2016). Rapid ascent and emplacement of basaltic lava during the 2005–06 eruption of the East Pacific Rise at ca. 9°51′N as inferred from CO₂ contents. *Earth and Planetary Science Letters*, 453, 152–160. https://doi.org/10.1016/j.epsl.2016.08.007
- Georgen, J. E., Lin, J., & Dick, H. (1998). Models of mantle upwelling beneath the Southwest Indian ridge: The effects of ridge-transform geometry on magma supply at an ultra-slow spreading ridge. Eos, Transactions, American Geophysical Union, 79, F854.
- Georgen, J. E., Lin, J., & Dick, H. J. (2001). Evidence from gravity anomalies for interactions of the Marion and Bouvet hotspots with the Southwest Indian Ridge: Effects of transform offsets. Earth and Planetary Science Letters, 187(3-4), 283-300. https://doi.org/10.1016/ s0012-821x(01)00293-x
- Girona, T., & Costa, F. (2013). DIPRA: A user-friendly program to model multi-element diffusion in olivine with applications to timescales of magmatic processes. Geochemistry, Geophysics, Geosystems, 14(2), 422–431. https://doi.org/10.1029/2012gc004427
- Grevemeyer, I., Hayman, N. W., Lange, D., Peirce, C., Papenberg, C., Van Avendonk, H. J. A., et al. (2019). Constraining the maximum depth of brittle deformation at slow- and ultraslow-spreading ridges using microseismicity. *Geology*, 47(11), 1069–1073. https://doi.org/10.1130/g46577.1

MA ET AL. 14 of 17

- Grove, T. L., Kinzler, R. J., & Bryan, W. B. (1992). Fractionation of mid-ocean ridge basalt (MORB). In Washington DC American geophysical union geophysical monograph series (Vol. 71, pp. 281–310).
- Gualda, G. A. R., Ghiorso, M. S., Lemons, R. V., & Carley, T. L. (2012). Rhyolite-MELTS: A modified calibration of MELTS optimized for silica-rich, fluid-bearing magmatic systems. *Journal of Petrology*, 53(5), 875–890. https://doi.org/10.1093/petrology/egr080
- Hartley, M. E., Morgan, D. J., Maclennan, J., Edmonds, M., & Thordarson, T. (2016). Tracking timescales of short-term precursors to large basaltic fissure eruptions through Fe–Mg diffusion in olivine. Earth and Planetary Science Letters, 439, 58–70. https://doi.org/10.1016/j. epsl.2016.01.018
- Herzberg, C. (2004). Partial crystallization of Mid-Ocean ridge basalts in the crust and mantle. *Journal of Petrology*, 45(12), 2389–2405. https://doi.org/10.1093/petrology/egh040
- Humler, E., & Whitechurch, H. (1988). Petrology of basalts from the Central Indian Ridge (lat. 25 23'S, long. 70 04'E): Estimates of frequencies and fractional volumes of magma injections in a two-layered reservoir. Earth and Planetary Science Letters, 88(1–2), 169–181. https://doi.org/10.1016/0012-821x(88)90055-6
- Ito, G., & Behn, M. D. (2008). Magmatic and tectonic extension at mid-ocean ridges: 2. Origin of axial morphology. Geochemistry, Geophysics, Geosystems, 9(9), 29. https://doi.org/10.1029/2008GC001970
- Jian, H., Singh, S. C., Chen, Y. J., & Li, J. (2017). Evidence of an axial magma chamber beneath the ultraslow-spreading Southwest Indian Ridge. Geology, 45(2), 143–146. https://doi.org/10.1130/g38356.1
- Kelley, D. F., & Barton, M. (2008). Pressures of crystallization of Icelandic magmas. *Journal of Petrology*, 49(3), 465–492. https://doi.org/10.1093/petrology/egm089
- Kvassnes, A. J., & Grove, T. L. (2008). How partial melts of mafic lower crust affect ascending magmas at oceanic ridges. Contributions to Mineralogy and Petrology, 156(1), 49–71, https://doi.org/10.1007/s00410-007-0273-x
- Langmuir, C. H. (1989). Geochemical consequences of in situ crystallization. Nature, 340(6230), 199-205. https://doi.org/10.1038/340199a0
- Lin, I. J., Chung, S.-L., Chu, C.-H., Lee, H.-Y., Gallet, S., Wu, G., et al. (2012). Geochemical and Sr–Nd isotopic characteristics of Cretaceous to Paleocene granitoids and volcanic rocks, SE Tibet: Petrogenesis and tectonic implications. *Journal of Asian Earth Sciences*, 53, 131–150. https://doi.org/10.1016/j.jseaes.2012.03.010
- Lissenberg, C. J., & MacLeod, C. J. (2016). A reactive porous flow control on Mid-ocean ridge magmatic evolution. *Journal of Petrology*, 57(11–12), 2195–2220. https://doi.org/10.1093/petrology/egw074
- Lissenberg, C. J., MacLeod, C. J., & Bennett, E. N. (2019). Consequences of a crystal mush-dominated magma plumbing system: A mid-ocean ridge perspective. *Philosophical Transactions Mathematical, Physical and Engineering Sciences*, 377(2139), 20180014. https://doi.org/10.1098/rsta.2018.0014
- Liu, Z., & Buck, W. R. (2023). The spreading rate dependence of the distribution of axial magma lenses along mid-ocean ridges. *Proceedings of the National Academy of Sciences*, 120(1), e2214048120, https://doi.org/10.1073/pnas.2214048120
- Lloyd, A. S., Ruprecht, P., Hauri, E. H., Rose, W., Gonnermann, H. M., & Plank, T. (2014). NanoSIMS results from olivine-hosted melt embayments: Magma ascent rate during explosive basaltic eruptions. *Journal of Volcanology and Geothermal Research*, 283, 1–18. https://doi.org/10.1016/j.jvolgeores.2014.06.002
- Ma, B., Liu, P.-P., Dick, H. J. B., Zhou, M.-F., Chen, Q., & Liu, C.-Z. (2023). Supplementary tables for 'trans-lithospheric ascent processes of the deep-rooted magma plumbing system underneath the ultraslow-spreading SW Indian ridge' [Dataset]. figshare. https://doi.org/10.6084/ m9.figshare.24347419.v2
- Macdonald, K. C., Scheirer, D. S., & Carbotte, S. M. (1991). Mid-ocean ridges: Discontinuities, segments and giant cracks. Science, 253(5023), 986–994. https://doi.org/10.1126/science.253.5023.986
- Maclennan, J. (2017). Bubble formation and decrepitation control the CO₂ content of olivine-hosted melt inclusions. Geochemistry, Geophysics, Geosystems, 18(2), 597–616. https://doi.org/10.1002/2016GC006633
- McDonough, W. F., & Sun, S. S. (1995). The composition of the Earth. Chemical Geology, 120(3), 223–253. https://doi. org/10.1016/0009-2541(94)00140-4
- Michael, P., Langmuir, C., Dick, H., Snow, J., Goldstein, S., Graham, D., et al. (2003). Magmatic and amagmatic seafloor generation at the ultraslow-spreading Gakkel ridge, Arctic Ocean. *Nature*, 423(6943), 956–961. https://doi.org/10.1038/nature01704
- Michael, P. J., & Cornell, W. C. (1998). Influence of spreading rate and magma supply on crystallization and assimilation beneath mid-ocean ridges: Evidence from chlorine and major element chemistry of mid-ocean ridge basalts. *Journal of Geophysical Research*, 103(B8), 18325–18356. https://doi.org/10.1029/98jb00791
- Montési, L. G. J., Behn, M. D., Hebert, L. B., Lin, J., & Barry, J. L. (2011). Controls on melt migration and extraction at the ultraslow Southwest Indian Ridge 10°–16°E. *Journal of Geophysical Research*, 116(B10), B10102. https://doi.org/10.1029/2011JB008259
- Moore, A., Coogan, L., Costa, F., & Perfit, M. (2014). Primitive melt replenishment and crystal-mush disaggregation in the weeks preceding the 2005–2006 eruption 9 50'N, EPR. Earth and Planetary Science Letters, 403, 15–26. https://doi.org/10.1016/j.epsl.2014.06.015
- Mutch, E. J. F., Maclennan, J., Shorttle, O., Edmonds, M., & Rudge, J. F. (2019). Rapid transcrustal magma movement under Iceland. Nature Geoscience, 12(7), 569–574. https://doi.org/10.1038/s41561-019-0376-9
- Nabelek, P. I., & Langmuir, C. H. (1986). The significance of unusual zoning in olivines from FAMOUS area basalt 527-1-1. Contributions to Mineralogy and Petrology, 93(1), 1–8. https://doi.org/10.1007/bf00963580
- Neave, D. A., & Maclennan, J. (2020). Clinopyroxene dissolution records rapid magma ascent. Frontiers in Earth Science, 8, 188. https://doi.org/10.3389/feart.2020.00188
- Newcombe, M. E., Plank, T., Barth, A., Asimow, P. D., & Hauri, E. (2020). Water-in-olivine magma ascent chronometry: Every crystal is a clock. Journal of Volcanology and Geothermal Research, 398, 106872. https://doi.org/10.1016/j.jvolgeores.2020.106872
- O'hara, M. (1977). Geochemical evolution during fractional crystallisation of a periodically refilled magma chamber. *Nature*, 266(5602),
- 503–507. https://doi.org/10.1038/266503a0
 O'Neill, H. S., & Jenner, F. E. (2012). The global pattern of trace-element distributions in ocean floor basalts. *Nature*, 491(7426), 698–704. https://
- Pan, Y., & Batiza, R. (2002). Mid-ocean ridge magma chamber processes: Constraints from olivine zonation in lavas from the East Pacific Rise at 9°30'N and 10°30'N. *Journal of Geophysical Research*, 107(B1), ECV9-1–ECV9-13. https://doi.org/10.1029/2001jb000435
- Patriat, P., & Segoufin, J. (1988). Reconstruction of the central Indian ocean. *Tectonophysics*, 155(1), 211–234. https://doi.org/10.1016/0040-1951(88)90267-3
- Peslier, A. H., Bizimis, M., & Matney, M. (2015). Water disequilibrium in olivines from Hawaiian peridotites: Recent metasomatism, H diffusion and magma ascent rates. *Geochimica et Cosmochimica Acta*, 154, 98–117. https://doi.org/10.1016/j.gca.2015.01.030
- Peslier, A. H., Woodland, A. B., & Wolff, J. A. (2008). Fast kimberlite ascent rates estimated from hydrogen diffusion profiles in xenolithic mantle olivines from southern Africa. *Geochimica et Cosmochimica Acta*, 72(11), 2711–2722. https://doi.org/10.1016/j.gca.2008.03.019

MA ET AL. 15 of 17

- Phipps Morgan, J., & Chen, Y. J. (1993). Dependence of ridge-axis morphology on magma supply and spreading rate. *Nature*, 364(6439), 706–708. https://doi.org/10.1038/364706a0
- Poore, H., White, N., & Maclennan, J. (2011). Ocean circulation and mantle melting controlled by radial flow of hot pulses in the Iceland plume. Nature Geoscience, 4(8), 558–561. https://doi.org/10.1038/ngeo1161
- Putirka, K. D. (2005). Mantle potential temperatures at Hawaii, Iceland, and the mid-ocean ridge system, as inferred from olivine phenocrysts: Evidence for thermally driven mantle plumes. Geochemistry, Geophysics, Geosystems, 6(5), O05L08, https://doi.org/10.1029/2005gc000915
- Putirka, K. D. (2008). Thermometers and barometers for volcanic systems. In *Reviews in mineralogy and geochemistry* (pp. 61–120). https://doi.org/10.2138/rmg.2008.69.3
- Reid, I., & Jackson, H. R. (1981). Oceanic spreading rate and crustal thickness. Marine Geophysical Researches, 5(2), 165–172. https://doi.org/10.1007/bf00163477
- Rhodes, J. M., Dungan, M. A., Blanchard, D. P., & Long, P. E. (1979). Magma mixing at mid-ocean ridges: Evidence from basalts drilled near 22°N on the Mid-Atlantic Ridge. *Tectonophysics*, 55(1–2), 35–61. https://doi.org/10.1016/0040-1951(79)90334-2
- Roeder, P. L., & Emslie, R. F. (1970). Olivine-liquid equilibrium. Contributions to Mineralogy and Petrology, 29(4), 275–289. https://doi.org/10.1007/BF00371276
- Rubin, K. H., & Sinton, J. M. (2007). Inferences on mid-ocean ridge thermal and magmatic structure from MORB compositions. *Earth and Planetary Science Letters*, 260(1–2), 257–276. https://doi.org/10.1016/j.epsl.2007.05.035
- Ruprecht, P., & Plank, T. (2013). Feeding andesitic eruptions with a high-speed connection from the mantle. *Nature*, 500(7460), 68–72. https://doi.org/10.1038/nature12342
- Sauter, D., Cannat, M., Rouméjon, S., Andreani, M., Birot, D., Bronner, A., et al. (2013). Continuous exhumation of mantle-derived rocks at the Southwest Indian Ridge for 11 million years, *Nature Geoscience*, 6(4), 314–320. https://doi.org/10.1038/ngeo1771
- Schlindwein, V., & Schmid, F. (2016). Mid-ocean-ridge seismicity reveals extreme types of ocean lithosphere. *Nature*, 535(7611), 276–279. https://doi.org/10.1038/nature18277
- Shaw, A. M., Behn, M. D., Humphris, S. E., Sohn, R. A., & Gregg, P. M. (2010). Deep pooling of low degree melts and volatile fluxes at the 85°E segment of the Gakkel Ridge: Evidence from olivine-hosted melt inclusions and glasses. *Earth and Planetary Science Letters*, 289(3–4), 311–322. https://doi.org/10.1016/j.epsl.2009.11.018
- Shen, Y., & Forsyth, D. W. (1995). Geochemical constraints on initial and final depths of melting beneath mid-ocean ridges. *Journal of Geophysical Research*, 100(B2), 2211–2237. https://doi.org/10.1029/94JB02768
- Singh, S. C., Crawford, W. C., Carton, H., Seher, T., Combier, V., Cannat, M., et al. (2006). Discovery of a magma chamber and faults beneath a Mid-Atlantic Ridge hydrothermal field. *Nature*, 442(7106), 1029–1032. https://doi.org/10.1038/nature05105
- Singh, S. C., Kent, G. M., Collier, J. S., Harding, A. J., & Orcutt, J. A. (1998). Melt to mush variations in crustal magma properties along the ridge crest at the southern East Pacific Rise. *Nature*, 394(6696), 874–878. https://doi.org/10.1038/29740
- Sinha, M., Constable, S., Peirce, C., White, A., Heinson, G., MacGregor, L., & Navin, D. (1998). Magmatic processes at slow spreading ridges: Implications of the RAMESSES experiment at 57 45' N on the Mid-Atlantic Ridge. *Geophysical Journal International*, 135(3), 731–745. https://doi.org/10.1046/j.1365-246x.1998.00704.x
- Soule, S. A., Nakata, D. S., Fornari, D. J., Fundis, A. T., Perfit, M. R., & Kurz, M. D. (2012). CO₂ variability in mid-ocean ridge basalts from syn-emplacement degassing: Constraints on eruption dynamics. *Earth and Planetary Science Letters*, 327–328, 39–49. https://doi.org/10.1016/j.epsl.2012.01.034
- Standish, J. J., Dick, H. J. B., Michael, P. J., Melson, W. G., & O'Hearn, T. (2008). MORB generation beneath the ultraslow spreading Southwest Indian Ridge (9-25°E): Major element chemistry and the importance of process versus source. *Geochemistry, Geophysics, Geosystems*, 9(5), Q05004. https://doi.org/10.1029/2008gc001959
- Sun, S.-S., & McDonough, W. F. (1989). Chemical and isotopic systematics of oceanic basalts: Implications for mantle composition and processes. *Geological Society, London, Special Publications*, 42(1), 313–345. https://doi.org/10.1144/gsl.sp.1989.042.01.19
- Tivey, M., Greene, J. A., Tominaga, M., Dick, H. J., Alodia, G., & Cheadle, M. J. (2019). Geophysical investigation of the Marion rise, southwest Indian ridge from the Discovery to Indomed fracture zones reveals vast exposures of mantle at the sea floor (p. T21D-0365).
- Wang, J., Su, B. X., Robinson, P. T., Xiao, Y., Bai, Y., Liu, X., et al. (2021). Trace elements in olivine: Proxies for petrogenesis, mineralization and discrimination of mafic-ultramafic rocks. *Lithos*, 388–389, 106085. https://doi.org/10.1016/j.lithos.2021.106085
- Wanless, V. D., & Behn, M. D. (2017). Spreading rate-dependent variations in crystallization along the global mid-ocean ridge system. *Geochemistry*, *Geophysics*, *Geosystems*, 18(8), 3016–3033. https://doi.org/10.1002/2017gc006924
- Wanless, V. D., & Shaw, A. M. (2012). Lower crustal crystallization and melt evolution at mid-ocean ridges. *Nature Geoscience*, 5(9), 651–655. https://doi.org/10.1038/ngeo1552
- Wanless, V. D., Shaw, A. M., Behn, M. D., Soule, S. A., Escartín, J., & Hamelin, C. (2015). Magmatic plumbing at Lucky Strike volcano based on olivine-hosted melt inclusion compositions. *Geochemistry*, *Geophysics*, *Geosystems*, 16(1), 126–147. https://doi.org/10.1002/2014gc005517
- Wessel, P., Luis, J. F., Uieda, L., Scharroo, R., Wobbe, F., Smith, W. H. F., & Tian, D. (2019). The generic mapping Tools version 6. *Geochemistry, Geophysics, Geosystems*, 20(11), 5556–5564. https://doi.org/10.1029/2019GC008515
- White, R. S., Minshull, T. A., Bickle, M. J., & Robinson, C. J. (2001). Melt generation at very slow-spreading oceanic ridges; constraints from geochemical and geophysical data. *Journal of Petrology*, 42(6), 1171–1196. https://doi.org/10.1093/petrology/42.6.1171
- Whitehead, J. A., Jr., Dick, H. J. B., & Schouten, H. (1984). A mechanism for magmatic accretion under spreading centres. *Nature*, 312(5990), 146–148. https://doi.org/10.1038/312146a0
- Yang, H.-J., Kinzler, R. J., & Grove, T. L. (1996). Experiments and models of anhydrous, basaltic olivine-plagioclase-augite saturated melts from 0.001 to 10 kbar. Contributions to Mineralogy and Petrology, 124(1), 1–18. https://doi.org/10.1007/s004100050169
- Yu, X., & Dick, H. J. B. (2020). Plate-Driven micro-hotspots and the evolution of the dragon Flag melting anomaly, southwest Indian ridge. Earth and Planetary Science Letters, 531, 116002. https://doi.org/10.1016/j.epsl.2019.116002
- Zellmer, G. F., Dulski, P., Iizuka, Y., & Perfit, M. R. (2012). Rates and processes of crystallization in on-axis and off-axis MOR basaltic melts. Lithos, 154, 1–15. https://doi.org/10.1016/j.lithos.2012.07.019
- Zellmer, G. F., Rubin, K. H., Dulski, P., Iizuka, Y., Goldstein, S. L., & Perfit, M. R. (2011). Crystal growth during dike injection of MOR basaltic melts: Evidence from preservation of local Sr disequilibria in plagioclase. *Contributions to Mineralogy and Petrology*, 161(1), 153–173. https://doi.org/10.1007/s00410-010-0518-y
- Zhou, H. Y., & Dick, H. J. B. (2013). Thin crust as evidence for depleted mantle supporting the Marion Rise. Nature, 494(7436), 195–200. https://doi.org/10.1038/nature11842
- Zhou, H. Y., Qian, S. P., & Dick, H. J. B. (2022). Explosive alkaline volcanism on the SW Indian ridge. https://doi.org/10.21203/rs.3.rs-1761254/v1

MA ET AL. 16 of 17

References From the Supporting Information

- Chakraborty, S. (2010). Diffusion coefficients in olivine, Wadsleyite and Ringwoodite. Reviews in Mineralogy and Geochemistry, 72(1), 603-639. https://doi.org/10.2138/rmg.2010.72.13
- Costa, F., Chakraborty, S., & Dohmen, R. (2003). Diffusion coupling between trace and major elements and a model for calculation of magma residence times using plagioclase. *Geochimica et Cosmochimica Acta*, 67(12), 2189–2200. https://doi.org/10.1016/s0016-7037(02)01345-5
- Costa, F., Dohmen, R., & Chakraborty, S. (2008). Time scales of magmatic processes from modeling the zoning patterns of crystals. Reviews in Mineralogy and Geochemistry, 69(1), 545–594. https://doi.org/10.2138/rmg.2008.69.14
- Costa, F., & Dungan, M. (2005). Short time scales of magmatic assimilation from diffusion modeling of multiple elements in olivine. *Geology*, 33(10), 837, https://doi.org/10.1130/g21675.1
- Dohmen, R., Becker, H.-W., & Chakraborty, S. (2007). Fe–Mg diffusion in olivine I: Experimental determination between 700 and 1,200°C as a function of composition, crystal orientation and oxygen fugacity. *Physics and Chemistry of Minerals*, 34(6), 389–407. https://doi.org/10.1007/s00269-007-0157-7
- Dohmen, R., & Chakraborty, S. (2007a). Fe–Mg diffusion in olivine II: Point defect chemistry, change of diffusion mechanisms and a model for calculation of diffusion coefficients in natural olivine. *Physics and Chemistry of Minerals*, 34(6), 409–430. https://doi.org/10.1007/s00269-007-0158-6
- Dohmen, R., & Chakraborty, S. (2007b). Fe–Mg diffusion in olivine II: Point defect chemistry, change of diffusion mechanisms and a model for calculation of diffusion coefficients in natural olivine. *Physics and Chemistry of Minerals*, 34(8), 597–598. https://doi.org/10.1007/s00269-007-0185-3
- Jambon, A., Lussiez, P., Clocchiatti, R., Weisz, J., & Hernandez, J. (1992). Olivine growth rates in a tholeiitic basalt: An experimental study of melt inclusions in plagioclase. Chemical Geology, 96(3-4), 277-287. https://doi.org/10.1016/0009-2541(92)90059-e
- Mallmann, G., & O'Neill, H. S. C. (2009). The crystal/melt partitioning of V during mantle melting as a function of oxygen fugacity compared with some other elements (Al, P, Ca, Sc, Ti, Cr, Fe, Ga, Y, Zr and Nb). *Journal of Petrology*, 50(9), 1765–1794. https://doi.org/10.1093/petrology/egp053
- Pearce, T. (1984). The analysis of zoning in magmatic crystals with emphasis on olivine. Contributions to Mineralogy and Petrology, 86(2), 149–154. https://doi.org/10.1007/bf00381841
- Shea, T., Costa, F., Krimer, D., & Hammer, J. E. (2015). Accuracy of timescales retrieved from diffusion modeling in olivine: A 3D perspective. American Mineralogist, 100(10), 2026–2042. https://doi.org/10.2138/am-2015-5163
- Wallace, G. S., & Bergantz, G. W. (2004). Constraints on mingling of crystal populations from off-center zoning profiles: A statistical approach. American Mineralogist, 89(1), 64–73. https://doi.org/10.2138/am-2004-0109

Erratum

In the originally published version of this article, coauthor Henry J. B. Dick was affiliated with Woods Hole Oceanographic Institution. He is now an independent researcher, and this notation has been added to his affiliations. This may be considered the authoritative version of record.

MA ET AL. 17 of 17